ECS The Electrochemical Society
Advancing solid state & electrochemical science & technology

Impact of Functional Groups in Reduced Graphene Oxide Matrices for High Energy Anodes in Lithium-Ion Batteries

To cite this article: S. Müllner *et al* 2023 *J. Electrochem. Soc.* **170** 070523

View the article online for updates and enhancements.

Impact of Functional Groups in Reduced Graphene Oxide Matrices for High Energy Anodes in Lithium-Ion Batteries

S. Müllner,[1,=,z] T. Held,[1,2,=] T. Tichter,[3] P. Rank,[2,4] D. Leykam,[1] W. Jiang,[5] T. Lunkenbein,[5] T. Gerdes,[2,4] and C. Roth[1,2,*]

[1]University of Bayreuth, Chair of Electrochemical Process Engineering, Bayreuth, Germany
[2]Bavarian Center for Battery Technology (BayBatt), Bayreuth, Germany
[3]Bundesanstalt für Materialforschung und -prüfung (BAM), Abt. Sicherheit von Gefahrgutverpackungen und Batterien, Berlin, Germany
[4]University of Bayreuth, Keylab Glass Technology, Bayreuth, Germany
[5]Department of Inorganic Chemistry, Fritz-Haber-Institut der Max-Planck-Gesellschaft, Berlin, Germany

Most high capacity anode materials for lithium-ion batteries (LiB) require a carbonaceous matrix. In this context one promising material is reduced graphene oxide (rGO). Herein, we present the influence of different reduction degrees of rGO on its physico-chemical properties, such as crystallinity, specific surface area, electrical conductivity and electrochemical lithiation/delithiation behavior. It is found that a heat treatment under inert and reducing atmospheres increases the long-range order of rGO up to a temperature of 700 °C. At temperatures around 1000 °C, the crystallinity decreases. With decreasing oxygen content, a linear decrease in irreversible capacity during cycle 1 can be observed, along with a significant increase in electrical conductivity. This decrease in irreversible capacity can be observed despite an increase in specific surface area indicating the more significant influence of the oxygen content on the capacity loss. Consequently, the reversible capacity increases continuously up to a carbon content of 84.4 at% due to the thermal reduction. Contrary to expectations, the capacity decreases with further reduction. This can be explained by the loss of functional groups that will be lithiated reversibly, and a simultaneous reduction of long-range order, as concluded from dq/dU analysis in combination with XRD analysis.

Graphene-based materials have attracted increasing attention as anodes for LiBs. This is essentially caused by their high electronic conductivity combined with a sufficient mechanical stability.[1,2] To date, pure graphene or graphene-like materials[3,4] as well as graphene-based nanocomposites (e.g. graphene in combination with high-capacity materials such as Si,[5,6] CuO[7] or Fe$_2$O$_3$[8]) have been proposed.

Graphene was firstly synthesized in 2004 by Novoselov et al. by using a mechanical exfoliation of graphite.[9] This preparation method is a primary example of a "top-down" process, where the desired carbon monolayers are generated by the mechanical treatment of graphite.[10]

An alternative "top-down" process starting from graphite involves so-called graphene oxide (GO) and allows to chemically produce graphene-like materials in large quantities at low costs.[11] GO is a partially oxidized, metastable, and non-stoichiometric carbon compound whose structure is not entirely known to date.[12] It is commonly prepared by using a modified Hummers' method,[13] where the oxidation is achieved by adding sodium nitrate, sulfuric acid and potassium permanganate to graphite. Followed by several washing steps with an aqueous solution of hydrogen peroxide or deionized water, pure GO is obtained. During the process, the oxidation step introduces oxygen-containing functional groups on and into the graphite structure. It is assumed that there are epoxide (C–O–C), singly bonded oxygen (C–O), and hydroxyl (C–OH) groups present at the surface.[14,15] Additionally, carbonyl groups (C=O) are expected to form at defect sites as well as carboxyl (O=C–OH), carbonyl and hydroxyl groups at the edges.[14,15] Associated with the formation of GO an expansion of individual graphitic layers up to the point of exfoliation takes place. Subsequently to exfoliation, graphene-like layers can be generated by various reduction pathways. The graphene-like material synthesized in this way is consequently named reduced graphene oxide (rGO). Typically, no single graphene layers but "rGO stacks" consisting of up to 4–6 layers are obtained.[16,17]

One possible way of reduction is a thermally induced reaction, where GO is heated in an inert or reducing atmosphere. This technique represents a simple, fast, safe and more economically viable alternative when compared to chemical, photochemical or biological reduction paths.[18]

Nevertheless, the thermal reduction of GO is a complex process in which the supply of heat triggers a multistage degradation or decomposition process.[19] It can be divided into four different temperature ranges:[19]

Stage I 25 °C–130 °C,
Stage II 140 °C–180 °C,
Stage III 180 °C–600 °C, and
Stage IV 600 °C–1000 °C.

In the first stage, an initial slow diffusion of intercalated water molecules (comparable to a drying process) takes place. The lattice spacing of the individual GO layers is only slightly reduced. In the second stage, the rapid escape of the forming gases—mainly H$_2$O - causes exfoliation of individual GO layers. Above 180 °C in stage 3, the removal of oxide groups, predominantly carboxyl groups, begins.[19] In addition to H$_2$O, also CO$_2$ and CO are formed here.[5] Thus, carbon atoms are removed from the graphene framework during the reaction and defects may remain or form.[15] During the reaction, a rearrangement of the oxygen-containing groups can occur, in which in particular phenolic groups are being formed.[20] Above 600 °C - in the final stage - hydroxyl and epoxide as well as residual carboxyl groups are removed.[11,19] In this temperature range, a re-formation of the aromatic structure occurs. Depending on the heating rate, the resulting rGO material can exhibit specific surface areas between 30 and 500 m^2 g^{-1}. The reason for this is whether the resulting product gases are released suddenly, disrupting the carbon matrix by sudden expansion, or whether they gradually emerge due to very low heating rates and do not thermally exfoliate the material.[21] However, temperatures above 1000 °C are necessary to achieve complete regraphitization.[20]

=Equal Contribution.
*Electrochemical Society Member.
zE-mail: sebastian.muellner@uni-bayreuth.de

Consequently, the oxygen content and the structure of rGO are strongly dependent on the reduction temperature or the reduction process. Generally, an increasing degree of reduction leads to a more graphene-like material and hence to an increase in specific energy density related to the desired lithiation reactions of polycyclic, aromatic hydrocarbons (graphite: 372 mAh g^{-1},[22] soft carbons: 200 mAh g^{-1} [23]).

However, it is assumed that functional groups, such as C=O and C–OH, can enhance reversible and fast Li storage.[24] In addition, the oxygen-containing functional groups have an influence on the irreversible loss of capacity, since irreversible parasitic reactions can take place in addition to the faradaic and reversible reactions with lithium. Other important parameters for the reversible lithiation process are the crystallinity as well as the long-range order. During the thermal reduction of GO, these parameters cannot be varied independently and therefore not considered individually.

To understand the correlation between the critical parameters and their influence on the electrochemical performance, in this work different (r)GO materials are investigated in terms of their elemental composition, type of functional groups, crystal structure and specific surface area. This includes the evaluation of the capacity loss in the first cycle, the stability and the total capacity over 100 cycles. A key aspect is the assignment of the different lithiation processes of (r) GO, either graphitic intercalation or a reaction with functional groups. Based on this holistic approach, conclusions can be drawn about the physico-chemical reasons for the predominant and capacity-determining effects. As a result, critical and decisive parameters are identified, so that the material can be tailored and adapted to different applications.

Experimental

Synthesis procedure.—Graphite oxide (GO, EXGO U98 300, *Graphit Kropfmühl*)), synthesized via a modified Hummer's method,[13] is dispersed and ultrasonically treated in fully demineralized water by *Future Carbon*. The GO particles were partially exfoliated by this ultrasonic treatment. A suspension of 1 wt% is reduced via reactive spray drying; details of our technique used here have already been published.[5] To achieve different degrees of reduction, the reactive spray dried rGO was heated in a tube furnace for 2 h under pure argon at 700 °C as well as in an argon/hydrogen atmosphere (95 Vol% Ar, 5 Vol% H$_2$) at 700 °C or 1000 °C. The used temperature ramp was 10 K min^{-1}.

Electrode preparation process.—Untreated GO and the different rGO materials are mixed with water, acetylene carbon black (CB, *CABOT*), sodium carboxymethyl cellulose (CMC, *Sigma Aldrich*) and styrene-butadiene rubber (SBR, *Zeon*) in a weight ratio of CMC: SBR = 1:1. The resulting ink consists of (r)GO active material, CB conductive additive and CMC/SBR binder in a ratio of 85:10:5 dispersed in water. The high amount of conductive additive is added to compensate the low electrical conductivity of the highly oxidized native/pristine GO. The slurry is diluted by adding water and using a planetary centrifugal mixer (ARE-250 CE, *Thinky*) for 10 min at 1600 rpm (mixing and defoaming mode for 5 min each) to obtain an ink with a viscosity of approximately 2 Pa s at a shear rate of 12.5 s^{-1} (resulting from wet film thickness and coating speed). It is wet coated on a copper foil (20 μm, *Schlenk*) using a doctor blade applicator (Zehntner, Modell: ZUA 200) to a wet film thickness of 400 μm at a speed of 5 mm s^{-1} on a film applicator (Erichsen, COATMASTER 509/MC-I). The electrodes are dried over night at room temperature in air in a drying chamber filled with silica-gel.

Half-cell assembly and cycling.—Before cell assembly the electrodes are punched out by an electrode cutter (El-Cut 12 mm, *El Cell*) to 12 mm coins and dried at 110 °C for 12 h in Ar atmosphere.

Subsequently, the batteries are assembled in an Argon filled glovebox (O$_2$ and H$_2$O content <1 ppm) in a coin-cell-type half-cell setup (Swagelok cell). 12 mm coins of lithium foil (750 μm, *Alfa Aesar*) are used as counter electrode and Whatman GF/C glass microfiber filter (125 μm, *Sigma Aldrich*) as a separator (d = 12.5 mm). To ensure constant pressure (0.05 MPa), a steel spring (EN-material number: 1.4310, *Gutekunst Federn*) and a nickel coin (d = 12 mm, h = 500 μm; *HMW Hauner*) is placed within the cell stack. A 1 M solution of LiPF$_6$ in a 1:1 (v/v) mixture of ethylene carbonate (EC) and dimethyl carbonate (DMC) (SelectityleTM LP 30, *BASF*) is used as electrolyte.

The galvanostatic cycling is performed for 100 cycles at a current density of 37.2 mA g^{-1} in a voltage range of U = 0.01 − 1.5 V for all materials under investigation. This current density is equivalent to a C-rate of 0.1 with respect to the theoretical capacity of graphite (LiC$_6$, 372 mAh g^{-1}).[22] The low current density was chosen to minimise the influence of the different physicochemical properties of the active materials and their effect on the electrode characteristics (e.g. thickness, porosity, and electrolyte wetting). The termination criterium of 1.5 V is selected to ensure comparability with standard graphite material. Furthermore, a larger voltage range could not be realized in the full-electrode design.

Physico- and electrochemical characterization techniques.— The scanning electron microscopy (SEM) characterization shown in this work is carried out with a Zeiss scanning electron microscope (model ULTRA-Plus) at an accelerating voltage of 3 kV. The elemental ratios for carbon (C), hydrogen (H), nitrogen (N), sulfur (S), and the correspondingly calculated oxygen (O) content are obtained to determine the degree of reduction of analysed (r)GO materials using EA 3000 from HEKAtech (CHNS elemental analysis). In addition, the crystal structure is characterized using an X-ray diffractometer (XRD, X'Pert MPD type: PW 3040/00, Philips Analytical). The measurements are performed in the range of 2θ = 10° − 90° with a step size of 0.02° at a scanning speed of 10 s at room temperature. To detect the asymmetric vibrations of molecular bonds in the investigated materials, a Fourier transform infrared (FT-IR) spectrometer (Bruker Tensor 27) with attenuated total reflection is used (Platinum-ATR). The specific surface area is determined via N$_2$-Physisorption using the Brunauer-Emmet-Teller method (BET) with ASAP 2010, from Micromeritics. The samples are dried at 80 °C. The particle size distributions and mean particle sizes d$_{50}$ of the materials are determined by static light scattering (SLS, Retsch LA-950, complex refractive index n = 2.71, k = 1,31).[25] TEM, STEM images, DF patterns and EDX spectrum were recorded by a ThermoFisher Scientific Talos F200X at the acceleration voltage 200 kV with FEI Ceta 16 M CMOS camera. Considering about the possible sensitivity of beam irradiation on carbon materials, HRTEM images were also acquired at 80 kV for comparison for one sample. Not only the morphology, but also layer distance, and layer numbers are consistent with the conclusions we get at 200 kV, thus confirming little effect from beam irradiation. The information limit of TEM and point resolution STEM of this microscope are 1.2 and 1.6 Å, respectively. The microscope was equipped with four silicon drift EDX detectors (SDDs) and an energy resolution of 130 eV. EDX quantification was performed using Velox software (Thermo Fisher). Selected aperture of 40 μm was chosen for selected area electron diffraction (SAED) at a camera length of 660 mm. C1 and C2 aperture at 2000 and 70 μm, gun lens 3, spot size 3/6, exposure time of 2 s and binning of 4 for images and DF patterns. Considering about the possible beam irradiation, HRTEM images was also obtained by JEOL ARM 200 F operated at 80 kV, equipped with CEOS CESCOR and CEOS CETCOR double spherical aberration correctors, and GATAN Oneview camera. Image mode operated at probe current of 0.045 nA and probe size of 0.1 nm. To improve the signal to noise ratio, multiple frames were taken within total 2 s and then summed up, with the online drift correction (GMS3, Thermo Fisher). Raman measurements were performed using an in-house built spectroscope (details are published by Zöllner and Brüggemann[26]) with a laser wavelength of 532 nm and power 10 mW in order to minimize the sample

changes. For X-ray photoelectron spectroscopy (XPS) analysis a SPECS PHOIBOS 100 analyzer using Al Kα X-ray excitation source (1486.74 eV) is used. The spectra are acquired using a step size of 0.05 eV, dwell time of 0.1 and a pass energy of 10 eV with 90 kV and 2200 kV bias and detector voltage, respectively. The electrical conductivities are measured via galvanostatic impedance spectroscopy (GEIS) using a Gamry Reference 600 in a frequency range from 1.000 to 10 Hz at a current of 0.05 mA. All measurements are performed in a universal testing machine (Instron Series 5569) under a compression of 1 MPa. Contact angle measurements are performed with the Drop Shape Analyzer Krüss DSA100 and the viscosity study with MCR 702 MultiDrive from Anton Paar using a one-plate-measuring system. The galvanostatic measurements are carried out at a BaSyTec CTS Lab test station. To be able to draw conclusions regarding the voltage-dependent capacity distribution, dq/dU characteristics are generated using an in-house built script for data processing. This routine applies a Savitzky-Golay filter and achieves an unconditionally stable smoothing according to a one-dimensional diffusion pulse by exploiting the semi-implicit Crank-Nicolson method. Details on the smoothing process can be found in the supplementary information.

Results and Discussion

SEM and CHNS elemental analysis.—As the graphene oxide becomes increasingly reduced, various physico-chemical properties change. Figure 1 illustrates the SEM images combined with the results of the CHNS elemental analysis for each (reduced) graphene oxide material investigated in this study.

Figure 1a/b show the pristine GO, where (a) represents the as received material and (b) the GO after ultrasonic treatment diluted in water (UST). The UST is the first step of the rGO synthesis procedure via reactive spray drying (RSD).[5] The dispersion is applied to a SEM sample holder and dried for further analysis. In its native state, GO shows a lamellar structure, similar to that of graphite. As a result of ultrasonic treatment and subsequent drying, the first layered structures can be detected in GO. However, exfoliation with a resulting change in structure is not observed. It is not entirely clear whether the individual layers are only formed during drying on the sample holder or whether the graphene oxide individual layers are present in dispersion. CHNS analysis gives an

oxygen content for GO of 25 at%, the highest of all materials analysed.

GO treatment in the reactive spray drying process reduces the oxygen content to 14 at% as a consequence of thermal reduction (Fig. 1c, rGO$_{RSD}$). During the rapid release of H$_2$O, CO$_2$, and CO gases,[5,27] the desired expansion of the individual graphene sheets takes place, resulting in the formation of pores in between the layers. Furthermore, RSD significantly reduces the amount of nitrogen and sulfur impurities within the material. This can be explained by a reaction with the released oxygen to form gaseous components such as NO$_x$ and SO$_x$.

Figure 1d/e/f show the rGO materials produced in the RSD reactor with different subsequent thermal reduction treatments. In general, the SEM images reveal only slight structural changes after thermal post-treatment. In Fig. 1d the results for rGO subsequently reduced in argon for 2 h at 700 °C are depicted (rGO$_{700Ar}$). The image indicates no major change in structure, while CHNS analysis confirms further reduction with a resulting oxygen content of less than 11 at%.

Figure 1e shows the results for rGO$_{700Ar/H2}$ which is reduced in argon/hydrogen atmosphere (Ar: 95 Vol%, H$_2$: 5 Vol%) at 700 °C for 2 h. Subsequently, the oxygen content in rGO$_{700Ar/H2}$ decreases significantly to 6 at% due to the reducing atmosphere. Moreover, the H-containing atmosphere leads to an increased hydrogen content of nearly 10 at%, the highest of all materials examined.

Figure 1f refers to the rGO post-treated in Ar/H$_2$ atmosphere for 2 h at 1000 °C (rGO$_{1000Ar/H2}$). The SEM image also shows a lamellar structure similar to the other post-treated rGO materials. Due to the increased reduction temperature, the oxygen content is reduced to 3 at%. Despite the Ar/H$_2$ atmosphere, the H content of only 4 at% is lower than for all other rGO materials (rGO$_{RSD}$, rGO$_{700Ar}$ and rGO$_{700Ar/H2}$).

In summary, thermal post-treatment at different temperatures and atmospheres successively changes the elemental composition, while it only slightly affects the morphology of rGO. A detailed list of the CHNS results is given in Table I.

XRD, BET, FTIR and Raman analysis.—SEM and CHNS analyses already demonstrate differences between the various rGO materials depending on the thermal post-treatment in terms of temperature and atmosphere. For a deeper insight, the influence of
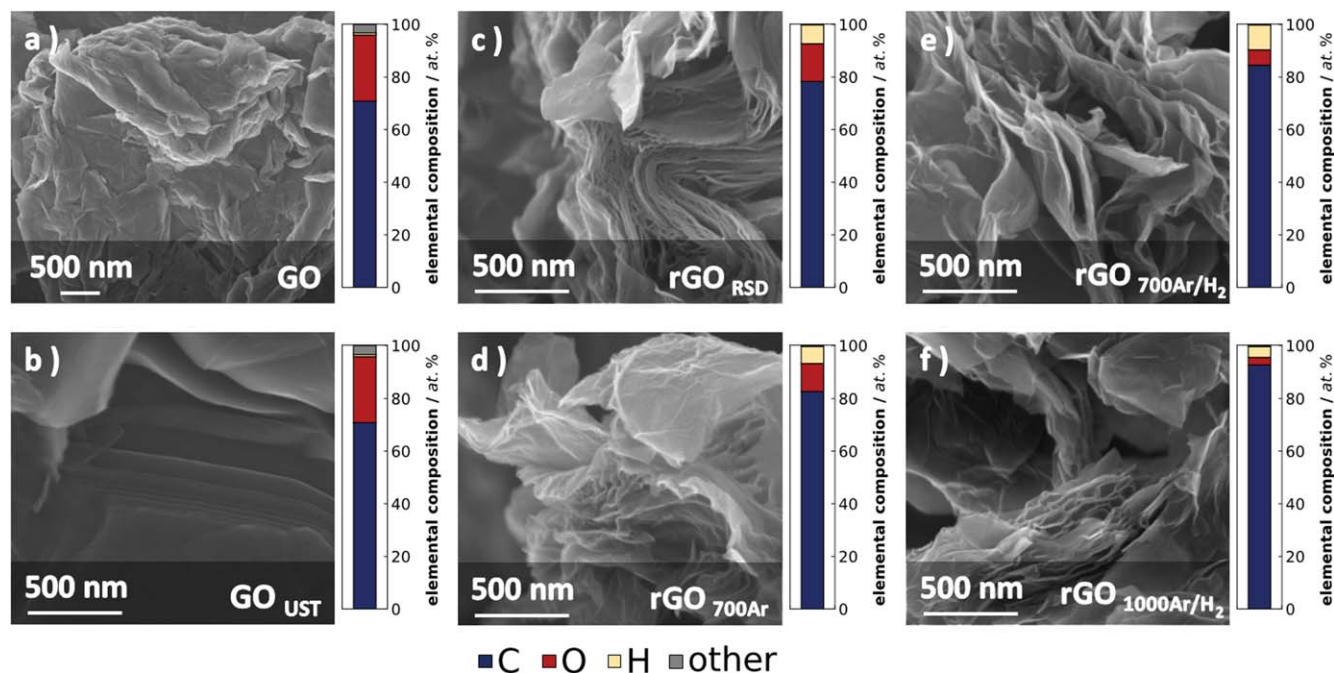

Figure 1. SEM images and CHNS analysis results for (a) GO, (b) ultrasonically treated GO$_{UST}$, (c) rGO$_{RSD}$, (d) rGO$_{700Ar}$, (e) rGO$_{700Ar/H2}$ and (f) rGO$_{1000ArH2}$.

Table I. Summary of the physico-chemical properties of GO, rGO_{RSD}, rGO_{700Ar}, $rGO_{700Ar/H2}$ and $rGO_{1000Ar/H2}$ from CHNS, BET, XRD, DLS, XPS and EIS analyses.

Method	Properties	Unit	GO	rGO_{RSD}	rGO_{700Ar}	$rGO_{700Ar/H2}$	$rGO_{1000Ar/H2}$
CHNS	C content	at%	70.8	78.3	82.7	84.4	92.8
	O content		25.1	14.3	10.6	5.9	2.8
	H content		0.8	7.2	6.4	9.5	3.9
	N content		2.6	0.1	0.2	0.1	0.1
	S content		0.6	0.1	0.2	0.1	0.4
BET	Surface area	$m^2\ g^{-1}$	48.2	90.0	132.7	109.3	76.8
XRD	Layer distance	Å	7.43	3.78	3.36	3.36	3.36
	$FWHM_{(001/002)}$	°2θ	1.0	4.0	0.8	0.7	2.5
SLS	d_{50}	μm	5.9	13.9	16.1	16.6	17.7
RAMAN	I_D/I_G ratio	—	1.04	1.06	0.99	1.00	1.44
	$FWHM_{D-band}$	cm^{-1}	157	183	166	140	140
XPS	C=C	at%	3.3	51.0	66.2	73.9	83.9
	π-π*		6.0	5.7	6.0	6.4	6.9
	C–C & C–H		4.9	22.7	13.3	9.8	2.7
	C–OH & C–O–C		44.5	13.7	9.8	6.3	3.9
	C=O		15.4	3.7	2.8	2.1	1.4
	O–C=O		25.9	3.2	1.9	1.4	1.2
EIS	El. conductivity	$S\ m^{-1}$	—	13.5	50.6	77.0	112.6

the thermal post-treatment on the crystallinity, the polar groups present on the carbon surface, the specific surface area as well as the inelastic Raman scattering will be discussed in the following. Figure 2 summarizes the results of XRD, FTIR-ATR, BET and Raman analysis for each (reduced) graphene oxide material.

From Fig. 2a the change in crystallinity of the material due to the thermal reduction can be monitored. As expected, GO is a highly crystalline material with a main (001) reflection at 11.8° (2θ) due to the increased interspacing layer between the (oxidized) graphene sheets (d_{GO} = 0.743 nm, calculated by Bragg's law) as a result of the presence of functional groups and trapped water within the carbon lattice.[5,33] In addition, GO shows a second strong reflection at 42.5°, which we attribute to the (111) plane of sp^3 hybridized carbon.[31] However, a superposition with the (100) reflection of sp^2 hybridized carbon at 43.0 is possible.

The reduction reaction during RSD significantly reduces the lattice spacing of the individual graphene layers, so that the main reflection shifts significantly towards the direction of higher angles for rGO_{RSD}, resulting in a lattice distance of 0.378 nm. In addition, overall crystallinity decreases due to the remaining lattice defects, which originate from the rapid heating during the RSD process. As a result, the full width at half maximum (FWHM) increases from 1° for GO to 4° for rGO_{RSD}. Re-graphitization at a high level cannot take place due to the short residence time in the furnace (in the range of seconds).[5] Furthermore, due to thermal reduction during the RSD process a conversion from sp^3 to sp^2 hybridisation takes place and the (111) reflection at 42.5° decreases. We attribute the remaining signal around 43° to the (100) reflection of sp^2 carbon.[32]

Thermal post-treatment for 2 h at 700 °C changes the long-range order of rGO_{700Ar} and $rGO_{700Ar/H2}$ considerably. Independent of the presence of hydrogen in the atmosphere, the long-range order increases significantly in both materials, resulting in FWHM values even lower than the starting material GO (see Table I). Therefore, it can be assumed that further elimination of oxygen-containing groups leads to a reconstruction of the graphitic structure. A shift of the peak maximum in the direction of larger angles, indicating a reduced lattice spacing, confirms this. The (002) lattice spacing is 0.336 nm for all post-treated rGO materials, which is very close to the theoretical value of graphite (0.334 nm[34]). In addition, as the turbostratic disorder gets less, the (101) reflection starts to appear at 45.3°.[35]

It is worth to note here, that an increase in reduction temperature ($rGO_{1000Ar/H2}$) leads to a further decrease of the O content (see Fig. 1) combined with a decrease in crystalline long-range order

(FWHM = 2.5 for $rGO_{1000Ar/H2}$). To verify whether the atmosphere has an influence on the XRD pattern at reduction temperatures of 1000 °C, rGO was also reduced at 1000 °C for 2 h in pure argon atmosphere. Furthermore, we investigated the influence of a 2 h temperature plateau at 700 °C before heating up to 1000 °C and holding again for 2 h. The results obtained correspond to that of $rGO_{1000Ar/H2}$ and are therefore not explicitly mentioned in Fig. 2a, but can be found in the supplementary information. In summary, neither the atmosphere (Ar or Ar/H₂), nor the temperature ramp, but the maximum temperature during the thermal post-treatment are critical parameters for the resulting crystallinity of rGO materials. A temperature of 1000 °C is not sufficient to achieve complete vacancy annihilation, resulting in a merging of adjacent overlapping layers, which results in continuous polycrystalline layers.[36,37]

In Fig. 2b FTIR spectra recorded under attenuated total reflection (ATR) are presented. In general, IR spectroscopy is suitable to detect a net change in the dipole moments of molecular bonds. In the case of (reduced) graphene oxide, this implies the oxygen-containing functional groups. Consequently, as the degree of reduction increases, the amount and intensity of the IR signals decrease as follows: GO > rGO_{RSD} > rGO_{700Ar} > $rGO_{700Ar/H2}$ > $rGO_{1000Ar/H2}$. A detailed discussion of the IR-active species in the GO starting material as well as in the reactive spray dried rGO_{RSD} has already been published.[5] In brief, after the RSD process only (asymmetric) C=C ($\nu \approx 1560\ cm^{-1}$ [5,38,39]), C–O–C ($\nu \approx 1215\ cm^{-1}$ [5,39,40]) and C=O ($\nu \approx 1730\ cm^{-1}$ [5,38,39]) bonds can be detected via ATR-FTIR spectroscopy. For rGO_{700Ar}, low intensities of C=C and C=O bonds can still be observed, while the rGO materials reduced in Ar/H₂ atmosphere do not show any significant IR-activity. We assume that the presence of hydrogen in the gas phase effectively reduces defects within the carbon lattice and thus eliminates asymmetric C=C and C–O–C bonds. Furthermore, the concentration of functional groups decreases with increasing degree of reduction and approaches the detection limits of the ATR-FTIR method. Since this technique primarily detects the IR-active groups on the surface, hydrogenation of carbons on the edge plane might be an important factor for the reduced IR-activity.

Figure 2c shows the N₂ physisorption (BET) characterization results. The starting material GO is ultrasonically treated during the manufacturing process and shows a specific surface area of 48 $m^2\ g^{-1}$ due to partial exfoliation. This exfoliation increases the fraction of freely accessible oxygen groups on the surface, which can be thermally reduced without a drastic volume expansion compared to the exfoliation of encapsulated oxygen groups.[41] During the
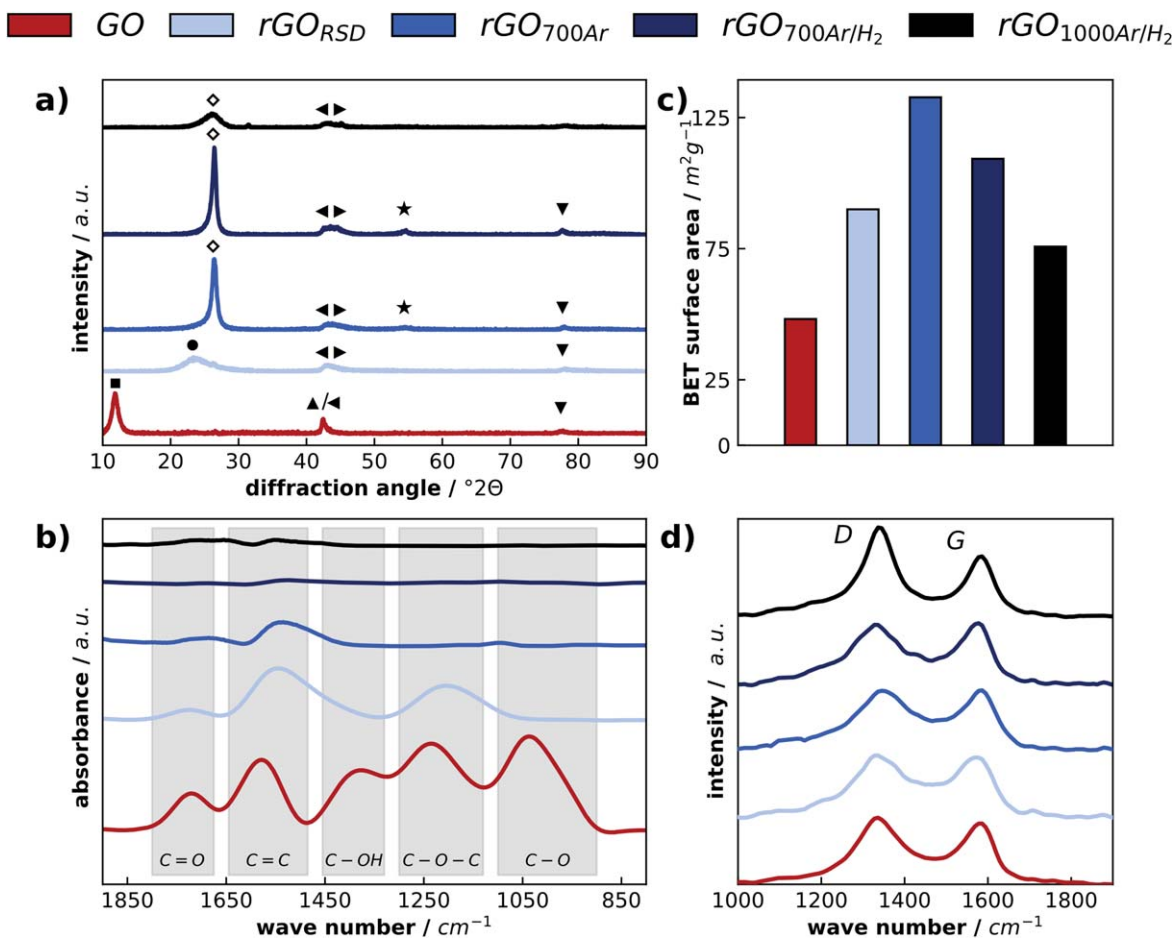
Figure 2. Results of the (a) XRD, (b) ATR-FTIR, (c) BET (N_2 physisorption) and (d) Raman analyses for GO, rGO_{RSD}, rGO_{700Ar}, $rGO_{700Ar/H2}$ and $rGO_{1000Ar/H2}$. In (a) the symbols correspond to the following lattice planes at 2θ: ■ = (001) non-reduced GO[28,29] at 11.9°, ▲ = (111) GO/diamond-like sp^3 [30,31] at 42.5°, ● = (002) partially reduced GO[28] at 23.5°, ◇ = (002) highly reduced GO/graphite[29,32] at 26.5°, ◄ = (100) rGO/graphite[32] at 43.0°, ► = (101) rGO/graphite[32] at 45.3°, ★ = (004) rGO/graphite[29,32] at 54.6°, ▼ = (110) rGO/graphite[32] at 77.7°.

reactive spray drying process, the GO gets thermally exfoliated but is not yet completely reduced. This is confirmed by the results of the XPS analysis (Fig. 4), the elemental analysis and in good agreement with the SEM images in Fig. 1c. Furthermore, the spray drying step results in the formation of rGO agglomerates, which in the end leads to a specific surface area of $90\,m^2\,g^{-1}$ for rGO_{RSD}. During the subsequent reduction, the remaining oxygen-containing groups are further reduced (Figs. 1e–1f), leading to continued exfoliation and thus to an increase in the specific surface area with a maximum of $133\,m^2\,g^{-1}$ at rGO_{700Ar}. Due to the prior exfoliation of the material in the RSD process despite a heating rate of 10 K min^{-1}, the surface enlargement is comparatively small to a thermal one-step reduction.[41]

The subsequent reduction of the specific surface area is probably due to a smaller number of defects distributed within the graphitic lattice, which allows the individual graphene layers to stack closer together. Consequently, an increase in temperature and the associated removal of lattice defects leads to a further decrease in the BET surface area for $rGO_{700Ar/H2}$ and $rGO_{1000Ar/H2}$. However, all measured specific surfaces areas for (r)GO materials are significantly higher compared to the standard anode material graphite but lower compared to rGO materials which are prepared by classic one-step thermal exfoliation, resulting in specific surface areas of 100 to $500\,m^2\,g^{-1}$.[21,41]

In Fig. 2d the results of the Raman spectroscopy for each (reduced) graphene oxide material are presented. The characteristic D (at 1350 cm^{-1})[42] and G (at 1580 cm^{-1})[42] bands for graphitic carbons can be seen for all materials. The D-peak would not be

visible in an ideal graphene structure due to crystal symmetries.[43] In this context, it can be said that as the number of defects or disorder increases, the Raman intensity of D and thus the I_D/I_G ratio increases. The I_D/I_G ratio of GO to rGO_{RSD} changes only slightly from 1.04 to 1.06. With thermal post-treatment at 700 °C in the course of healing of defects, I_D/I_G decreases to 1.00 ($rGO_{700Ar/H2}$) and 0.99 (rGO_{700Ar}), respectively. The simultaneous decrease in the FWHM of the D-band from 183 cm^{-1} for rGO_{RSD} to 166 cm^{-1} for rGO_{700Ar} to 140 cm^{-1} for $rGO_{700Ar/H2}$ is another indication of increase in structural order.[44] By further increase of the temperature to 1000 °C, the I_D/I_G ratio increases significantly to 1.44, which is consistent with the loss of long-range order crystallinity obtained from XRD. Oschatz et al. reported for nanostructured carbide-derived carbons that pyrolysis at temperatures of 1000 °C induces highly ultra-microporous defect structures by reducing the spaces between the graphene sheets.[44] They further note that temperatures above 1000 °C are necessary for a rearrangement into stacked layers with less micropores and continuous domains.[44] We observed that the graphene-like material here, obtained from the graphene oxide, behaves similarly.

Next to the characterizations presented in Fig. 2, the particle size distributions of the materials are investigated via static light scattering (SLS). Hereby a trend of increasing particle coarsening can be detected; the determined d_{50} values can be found in Table I. As the degree of reduction increases, the particle sizes increase as follows: $GO < rGO_{RSD} < rGO_{700Ar} < rGO_{700Ar/H2} < rGO_{1000Ar/H2}$. The main reason for that behaviour is the exfoliation of individual graphene layers as a result of the gas evolution during the reduction

reaction as well as the decreasing hydrophilic functionalization on the particle surface. This leads to a shift of the maximum in the particle size distribution towards larger diameters in the SLS analysis (theory of spherical particles). In addition, a bimodal distribution is emerging. The high temperatures during the reduction of GO lead to particle coarsening (Ostwald ripening).[45]

In good agreement with the results of the elemental analysis, the thermal post-treatment also alters the content of oxygen-containing functional groups detectable by FTIR spectroscopy. Although only a slight change in the morphology of the post-treated rGOs can be seen in the SEM (see Fig. 1, a significant change in the long-range order as well as in the specific surface area can be detected. These parameters are known to have a strong influence on the electrochemical behavior of the investigated material.

TEM and SAED analysis.—In order to confirm the rather surprising long-range order crystallinity loss during the thermal post-treatment from 700 °C to 1000 °C, TEM and SAED investigations were performed for all samples (Fig. 3).

The low magnification TEM images for all (r)GO samples show a typical two-dimensional nanosheet feature of graphite flakes (Figs. 3a–3e). Selected area electron diffraction was obtained to verify the atomic structure along the {001} zone axis. A series of diffraction rings, indexed by hexagonal structure, corresponds to the planes of (002), (100) (110), respectively.

From the TEM images (Figs. 3a–3e), the edge-on view thickness of the sheets can roughly reflect the stacked layer numbers. The rGO_{700Ar} and $rGO_{700Ar/H2}$ shows a higher stacked layer number than the others, consistent with the more pronounced XRD reflections at 26.5° for (002) planes. The high-magnification images (Figs. 3f–3j) confirm the interlayer spacing of 0.35 to 0.40 nm. The layer distance of the (002) planes are larger for GO and rGO_{RSD} (0.38–0.40 nm) but shrink after heat treatment at 700 and 1000 °C (0.33 − 0.36 nm), consistent with the different (002) reflections in XRD (see Fig. 2a). This observation also correlates with the decrease in the $FWHM_{D-band}$ from the Raman measurements (see Table I) and supports the hypothesis of an increase in long-range order at these reduction steps. The seeming conflict that the lower interlayer spacing of GO by TEM (0.40 nm) as compared to that by XRD (0.74 nm) can be explained by the evaporation of intercalated solvent molecules due to the high vacuum conditions as well as the electron beam radiation[46] during the TEM measurements. At the same time, the inside of the (002) rings in SAED are distinct. The intensity of rGO_{700Ar} and $rGO_{700Ar/H2}$ are higher than GO and $rGO_{1000Ar/H2}$, indicating their more stacked layers. While the diameter of the ring in rGO_{RSD} is smaller than the others, indicating larger d spacing of (002) planes, which is 0.38 nm for rGO_{RSD} compared with 0.33 nm for the ones post-treated at high temperatures. Despite the same d spacings from $rGO_{1000Ar/H2}$ to rGO_{700Ar} and $rGO_{700Ar/H2}$, we for $rGO_{1000Ar/H2}$ significantly less scattered signals in the (002) plane are observed. In conclusion, the combination of TEM and SAED confirms our findings in XRD and Raman of a decreased crystallinity of the post-treated sample at 1000 °C.

XPS and electrical conductivity measurements.—Since the FTIR analysis can detect the decreasing concentration of functional groups in the (reduced) graphene oxide materials only qualitatively, we additionally performed XPS measurements. The degree of reduction plays a decisive role for the electrical conductivity of rGO.[47] Figure 4 shows the results of the XPS and electrical conductivity measurements for all materials investigated.

Figure 4a shows the results of the XPS analysis regarding carbon 1s excitation; the detailed C 1s spectra can be found in the supplementary information in Fig. S2. The proportion of carbon not bound to an oxygen atom in graphene oxide is less than 15 at%. After RSD processing, this fraction increases significantly to 79 at% for rGO_{RSD}. The remaining share can mainly be attributed to C–O–C and C–OH bonds (14 at%); additionally, 4 at% are found for C=O and O–C=O, respectively. All oxygen-containing bonds (C–OH,

C–O–C, C=O, and O–C=O) decrease by increasing degree of reduction as follows: GO > rGO_{RSD} > rGO_{700Ar} > $rGO_{700Ar/H2}$ > $rGO_{1000Ar/H2}$. The same decreasing trend applies to the C–C single bond, except for the starting material GO. As the reduction proceeds, C=C double bonds as well as the π-π* system are formed successively. In Table I the XPS results are given in detail.

The changes in the carbon bonds have a significant influence on the electrical conductivity of the materials. Figure 4b illustrates the results of the conductivity measurements at room temperature as a function of the oxygen content. The dashed line serves to guide the eyes. In order to keep the influence of possibly different bulk densities low, all powders are loaded with 1 MPa in a universal testing machine during the measurements. As expected, there is a clear trend of increasing electrical conductivity with decreasing oxygen functionalization: GO < rGO_{RSD} < rGO_{700Ar} < $rGO_{700Ar/H2}$ < $rGO_{1000Ar/H2}$. Releasing oxygen from functional groups, the graphene oxide lattice, which is rich in sp^3 hybridisation, converts into a graphene-like sp^2 hybridized structure.[47] Due to the restoration of sp^2 hybridizations, its conductivity increases.[47] At room temperature graphene oxide is an insulating (to semi-conducting) material.[48,49] Therefore, no electrical conductivity could be measured for GO with our set-up ($<10^{-7}$ S m^{-1} [49]). After thermal reduction the electrical conductivity rises continuously to 14 (rGO_{RSD}), 51 (rGO_{700Ar}), 77 ($rGO_{700Ar/H2}$), and 113 S m^{-1} ($rGO_{1000Ar/H2}$), respectively. It is known that large crystal defects, such as multi-atomic voids, in the rGO lattice lead to moderate conductivities at room temperature.[47] Thermal post-treatment reduces these defects and thus increases the electrical conductivity.[47,50] These results are in good agreement with the XPS, FTIR, and CHNS analyses as well as with current literature.[47] Hence, an increasing electrochemical performance with decreasing defect structures would be expected.

Table I gives an overview of the most important physicochemical properties of all active materials. However, the deviation from the expected behavior based on these properties can be used to investigate the influence of the different functional groups on the cycling behavior and long-term stability, as discussed below.

Electrode characterization and electrolyte accessibility.—For further electrochemical characterization, the different active materials must be processed into electrodes. Here, it has been observed that the higher the amount of functional groups, the more water is required in the ink to achieve the necessary viscosity. This can be attributed to the interaction of the solvent water with the polar functional groups on the surface. As the degree of oxidation of (r) GO decreases, the required water amount decreases from 4.2 (GO) to 2.4 (rGO_{RSD}) to 2.1 (rGO_{700Ar}) to 2.0 ($rGO_{700Ar/H2}$) to 1.9 g_{H2O} g^{-1}_{AM} ($rGO_{1000Ar/H2}$). Due to the different water contents in the inks, the dry film thickness as well as the porosity of the electrodes cannot be kept constant. The average dry film thicknesses are as follows: GO = 61 μm, rGO_{RSD} = 134 μm, rGO_{700Ar} = 180 μm, $rGO_{700Ar/H2}$ = 184 μm and $rGO_{1000Ar/H2}$ = 201 μm. As a result, the areal mass loadings differ dependent on the functionalisation of the (r)GO material from 2.1 to 5.3 mg cm^{-2}. SEM images of the fresh electrodes can be seen in Fig. S5 in the supplementary information. However, this would have a decisive influence on the capacity that can be achieved at high current densities. To take this issue in consideration, all cycling tests presented are performed at a very low current density.

In order to test whether the different degrees of reduction of the active materials influence the wettability and thus the accessibility of electrolyte at the electrode surface, contact angle measurements are performed using pure dimethyl carbonate (DMC) as solvent. Contact angles of less than 11° are measured for all the electrodes, so it can be assumed that the electrolyte is sufficiently accessible.[51–53] Interestingly, no contact angle at all can be measured for both GO and $rGO_{1000Ar/H2}$. This is to be expected for $rGO_{1000Ar/H2}$, since the smallest amount of functional groups is present here, making the surface non-polar. For GO, this is rather surprising and could be due to the high porosity of the electrode as a result of the high water
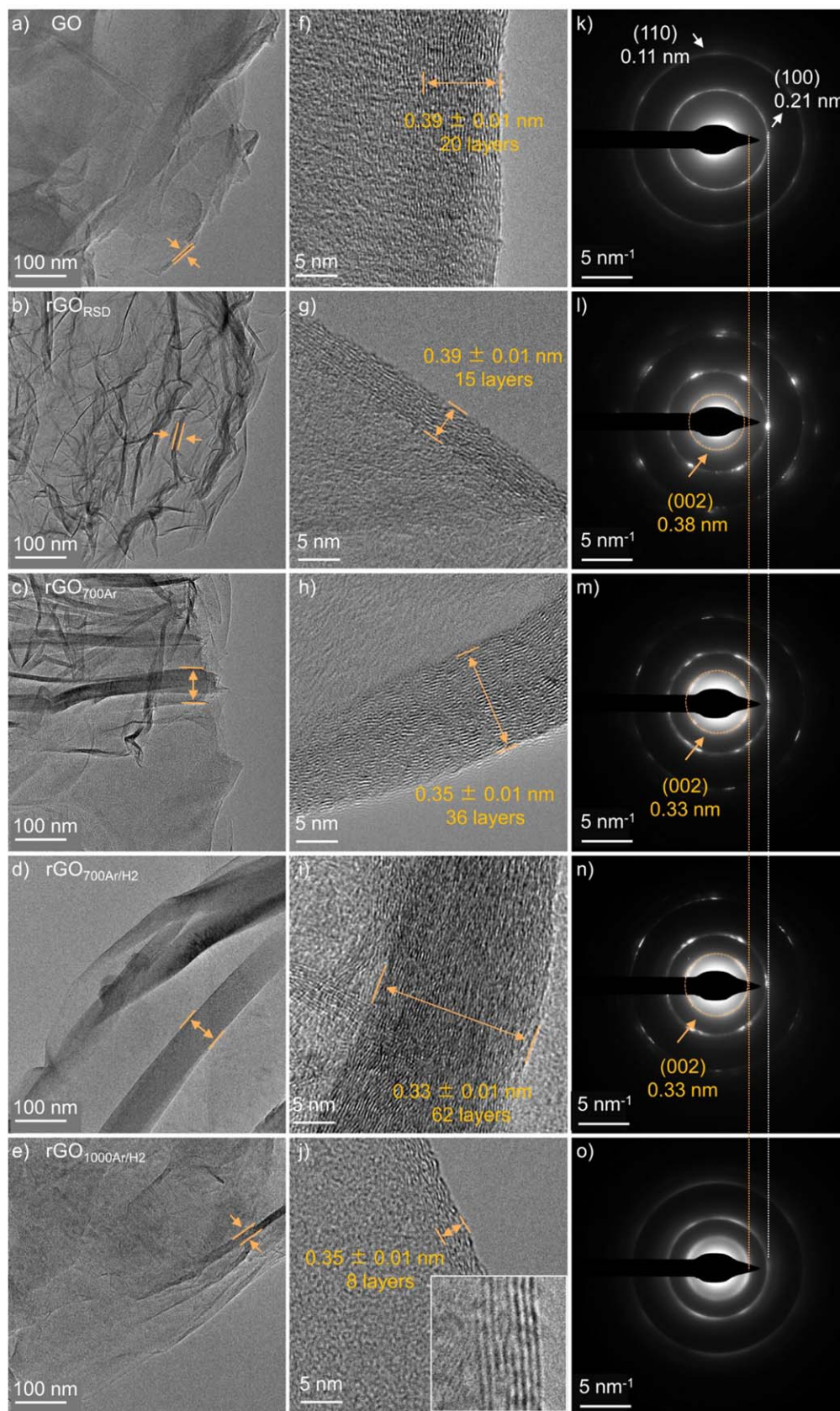
Figure 3. TEM and SAED images of (a)/(f)/(k) GO, (b)/(g)/(l) rGO$_{RSD}$, (c)/(h)/(m) rGO$_{700Ar}$, (d)/9i)/(n) rGO$_{700Ar/H2}$ and (e)/(j)/(o) rGO$_{1000Ar/H2}$.

content of the ink. For the other active materials, contact angles of 10.9° for rGO$_{RSD}$, 10.5° for rGO$_{700Ar}$ and 10.0° for rGO$_{700Ar/H2}$ could be determined.

Electrochemical characterization.—The results of the contact angle measurements and the corresponding adjustment to low current densities allow for an accurate analysis of the electrodes
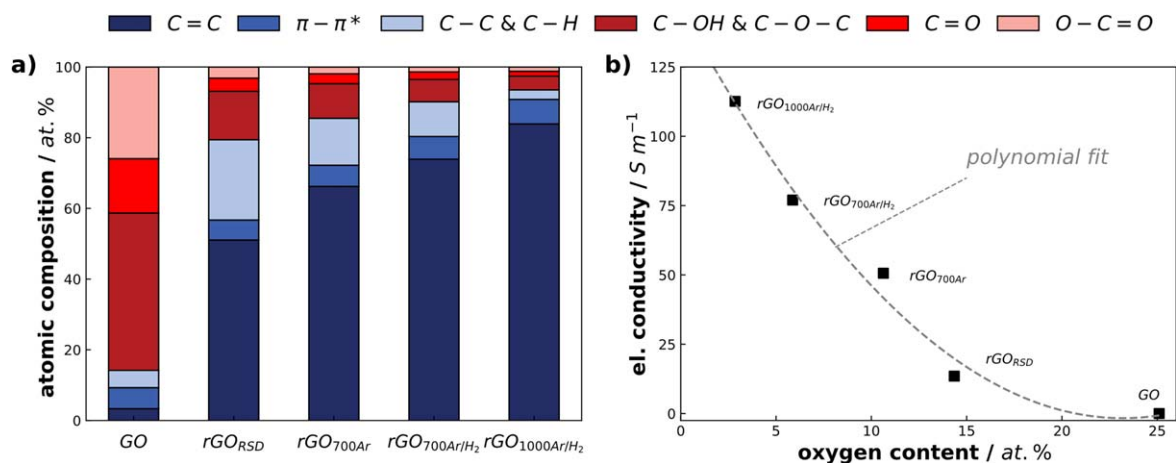
Figure 4. Results of the (a) XPS analysis and (b) electrical conductivity measurements over the oxygen content for GO, rGO_RSD, rGO_700Ar, rGO_700Ar/H2 and rGO_1000Ar/H2.

by galvanostatic cycling in a half-cell setup vs lithium as counter electrode. Figure 5 shows the capacities over 100 full cycles for each material as well as the irreversible portions in cycle 1 and 2.

In Fig. 5a the specific delithiation capacities are compared. Except for rGO_1000Ar/H2, which shows a reversible capacity at a low level around 200 mAh g^{-1}, the capacity increases by increasing reduction degree: GO < rGO_RSD < rGO_700Ar < rGO_700Ar/H2. All these active materials show a significant capacity drop of approximately 200 mAh g^{-1} during the first 20 cycles. In the further course of the experiment, a stable cycling behaviour is established at different levels of the specific capacity. We assume that the semi-reversible capacity at the beginning of the cycling is due to lithiation of the accessible functional groups. The capacity plateau reached after 50 cycles then mainly depends on the carbon framework and the intercalation of lithium in between the graphitic layers to form LiC_6, as this lithiation reaction of carbon is known to be highly reversible.[54,55] As the carbon ratio increases with increasing degree of reduction, the reversible capacities also increase. For a more detailed perspective, Fig. S4 in the supplementary information shows the capacity curves for cycles 1, 2, 10, 25, 50 and 100. Interestingly, rGO_700Ar and rGO_700Ar/H2 achieve the same reversible delithiation capacity from cycle 50 onwards. This indicates that the hydrogen-containing atmosphere during the thermal post-reduction affects the graphitic lattice much less than the end groups on the edge planes of rGO; the XRD results confirm this (see Fig. 2a). In agreement with previous studies,[54,56] our results demonstrate that increasing the hydrogen content increases and extends this (semi-) reversible capacity for approximately 50 cycles.

We assume that this trend cannot be explained by an increased healing of the defect sites due to the increased hydrogen content, but rather by the substitution of oxygen- by hydrogen-terminated carbons, since these can be (de-) lithiated more reversibly.

Furthermore, the cycling behavior of rGO_1000Ar/H2 differs significantly from the other active materials. No capacity drop can be observed during the first cycles due to the low content of oxygen-containing functional groups. Instead, the characteristic cycling behavior for soft carbons can be observed.[57,58] In general, the cycling behavior of rGO_1000Ar/H2 is very similar to that of other carbonaceous raw materials treated at temperatures around 1000 °C, such as petroleum pitches, polyvinyl chloride, or polyvinylidene fluoride.[59,60] XRD measurements show disorder in the crystalline structure (see Fig. 2a), which may be the main cause of the significantly lower specific capacity compared to graphite.[60]

Figure 5b shows the irreversible capacities ($c_{irr} = c_{lith} - c_{delith}$) in cycle 1 and 2 as a function of the oxygen content. In both cycles, a linear trend of increasing irreversible capacity with increasing oxygen content can be observed. For a more detailed examination, the capacity curves from Fig. S4a (in the supplementary information) can be considered. They show the irreversible capacity changes of the individual materials in cycle 1, which corresponds to the capacity loss during formation. There is a decreasing trend as a function of oxygen content in the carbon matrix as shown in Fig. 5b. The high irreversible capacity in the first cycle is due to the formation of the solid electrolyte interphase (SEI), where the electrolyte components react with the carbonaceous surface. The functional groups on (reduced) graphene oxide seem to have a major
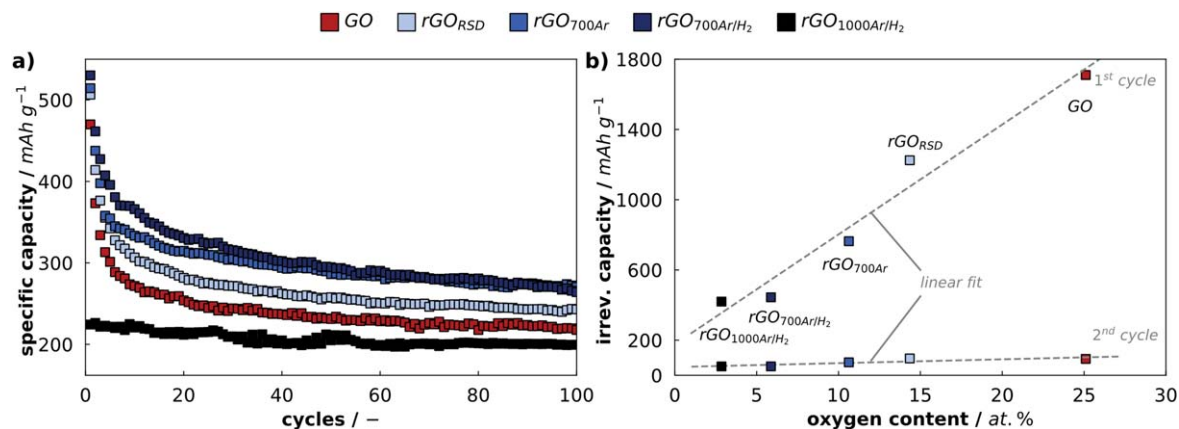

Figure 5. (a) Specific delithiation capacities (vs Li/Li$^+$) over 100 cycles and (b) irreversible capacities in cycle 1 and 2 for GO, rGO_RSD, rGO_700Ar, rGO_700Ar/H2 and rGO_1000Ar/H2 at a current density of 37 mA g^{-1}.

influence on the extent of SEI formation, leading to a massive irreversible capacity of 1710 mAh g^{-1} for GO. In contrast, for the most reduced active material rGO$_{1000Ar/H2}$ only a quarter of the irreversible capacity compared to GO is observed. This demonstrates that a major part of the oxygen-containing functional groups exhibits a non-reversible capacity by forming COOLi from –COOH and OLi from –OH groups.[54,55] Post-mortem XPS measurements of the C 1s and the O 1s spectra (see Fig. S3 in the supplementary information) of the cycled and delithiated electrodes confirm this hypothesis. Here, significantly higher intensities for both inactive Li$_x$C (at ∼283 eV[61,62]) and O$_x$Li$_y$/OH-Li (at ∼530 eV[63,64]) can be found for the materials exhibiting high oxygen functionalities. Interestingly, the fraction of Li$_x$C increases slightly again from rGO$_{700Ar/H2}$ to rGO$_{1000Ar/H2}$, contrary to the trend (GO > rGO$_{RSD}$ > rGO$_{700Ar}$ > rGO$_{700Ar/H2}$), showing that not exclusively functionalization but also long-range order crystallinity plays a role here. In the second cycle, the same trend can be observed at a much lower level. However, the irreversible capacity is very high for all materials, which is due to their high specific surface areas. The difference in BET surface area between the individual materials seems to be no longer decisive.

Despite a similar specific surface area of rGO$_{RSD}$ and rGO$_{1000Ar/H2}$, the irreversible capacity of rGO$_{RSD}$ during the first cycle is significantly higher. Consequently, the functional groups have a higher impact on the capacity loss than the electrode-electrolyte contact facilitated by high surface area. This can be confirmed by considering the lithiation plateaus of the investigated materials (see Fig. S4a, supplementary information). Thus, the lithiation capacity shifts with decreasing oxygen content from capacities above 1.0 V to lower values more typical of graphitic intercalations.

According to a better resolution of the slope changes from Figs. S4a–S4f, the dq/dU analyses (detailed explanation can be found in the supplementary information including the smoothing procedure) are interpreted below. The differential capacity plots in Fig. 6 provide a deeper insight in the origin and the reversibility of the respective capacity.

During the first cycle (Fig. 6a), only for graphite oxide a reaction around 2 V (vs Li/Li$^+$) can be detected. This potential is significantly higher than the ones known for SEI formation of the EC/DMC electrolytes on typical carbonaceous anode materials, such as graphite (beginning at less than 1 V vs Li/Li$^+$).[65,66] We assume that H$_2$O trapped within the GO sheets reacts with the electrolyte component in the potential range between 2.5 V and 1.5 V. Lundström et al. recently reported that EC ring opening is initiated by OH$^-$ originating from H$_2$O reduction reaction and/or oxygenic carbon surface groups in this potential range.[67] In addition to this strong capacity peak, a reduction of the electrolyte takes place at voltages between 1.5 V and 0.8 V. This phenomenon can be correlated with the number of oxygen-containing groups in the

active material. As the O content decreases, the potential at which the SEI begins to form shifts to lower values, which agrees well with previously reported studies.[56] As a result of the ongoing reaction with functional groups, the differential capacity for GO does not drop to zero (between 1.5 V and 0.8 V). At typical SEI formation potentials of 0.8 V, GO shows only a small peak in capacity, indicating that a passivation layer has already formed during the reaction at higher potentials.

In addition, the differential capacity signal resulting from the SEI formation partially overlaps with the reaction of the functional groups which keeps going on in this voltage range. At 0.4 V, the highest differential capacity can be detected for GO. This reaction is partially reversible, as it can be detected with lower intensity in the second cycle (Fig. 6b). Here, a semi-reversible lithiation with oxygen-containing functional groups on the surface seems to take place, which is consistent with previous studies.[68] Further we conclude this from the fact that the peak decreases with decreasing O content. At even lower potentials <0.25 V, reversible Li$^+$ intercalation occurs within the carbon lattice.

During delithiation, a significant voltage hysteresis can be observed for GO with a capacity peak above 1 V. Large voltage hystereses have been reported in the literature for hydrogen-containing carbonaceous materials,[69,70] which are most evident for GO, but also for rGO$_{RSD}$, rGO$_{700Ar}$ and rGO$_{700Ar/H2}$. One cause of this hysteresis can be the conversion from sp^2 to sp^3 hybridization of H-terminated carbon during the (de-) lithiation reaction.[70] Furthermore, GO has the lowest electrical conductivity (see Fig. 4b). This can increase the hysteresis effect due to the higher internal resistance of the active material.

In general, SEI formation starts at higher potentials (vs Li/Li$^+$) with increasing oxygen functionalization. In addition, the total electron consumption during SEI formation (integral under the curves in Fig. 6) decreases with increasing degree of reduction leading to a lower irreversible capacity (see Fig. 5b). This is a consequence of the following (irreversible) capacity trends at both 0.8 and 0.4 V: rGO$_{RSD}$ > rGO$_{700Ar}$ > rGO$_{700Ar/H2}$. Below 0.25 V, these three materials do not differ significantly. The delithiation curves do not deviate strongly, but the observed potential hysteresis decreases as the proportion of functional groups decreases from rGO$_{RSD}$ to rGO$_{700Ar}$ to rGO$_{700Ar/H2}$. In cycle 2 (Fig. 6b), the lithiation of these three materials is very similar.

The delithiation curves of rGO$_{RSD}$, rGO$_{700Ar}$, rGO$_{700Ar/H2}$ only slightly differ, as all of them again show a differential capacity plateau at potentials above 0.75 V which is related to the reaction of the functional groups on the carbon surface with lithium.

rGO$_{1000Ar/H2}$ performs quite differently during the (first) lithiation than all the other materials. Here, typical SEI formation can be detected starting from 1 V with its peak around 0.8 V. After that, there is a slow, but steady increase in capacity, which is highly reversible, as it can be seen in the second cycle (Fig. 6b). No
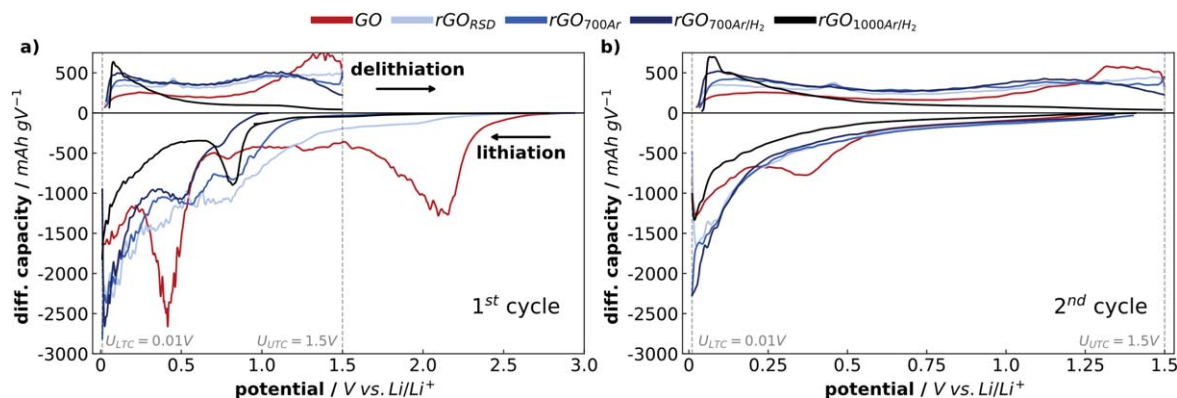

Figure 6. Specific differential capacities over the potential in a) cycle 1 and b) cycle 2 for GO, rGO$_{RSD}$, rGO$_{700Ar}$, rGO$_{700Ar/H2}$ and rGO$_{1000Ar/H2}$ at a current density of 37 mA g^{-1} (U$_{LTC}$ = lower termination criterion and U$_{UTC}$ = upper termination criterion).
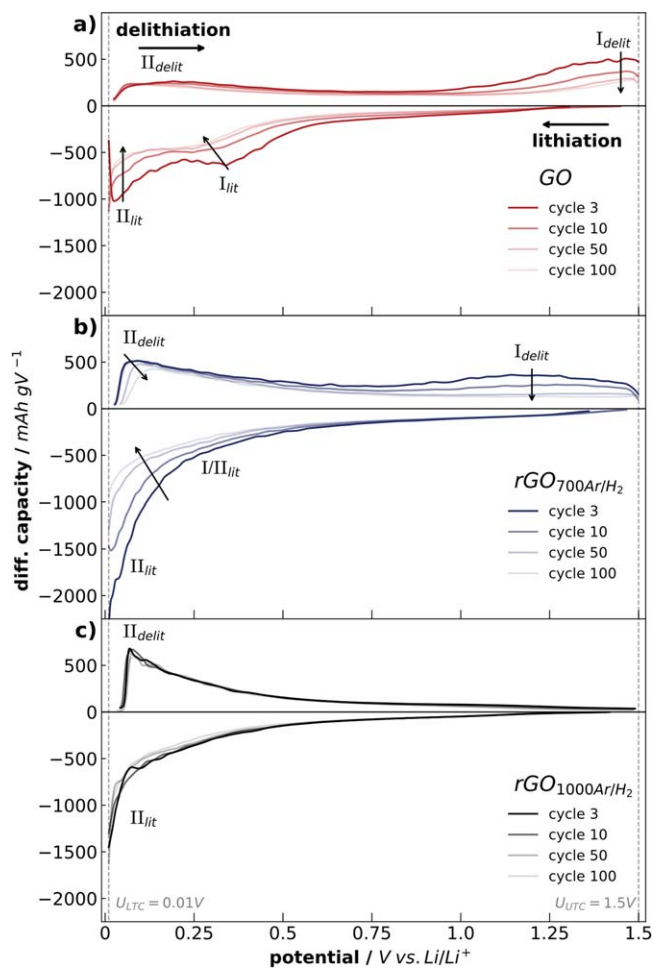
Figure 7. Specific differential capacities over potential in cycle 3, 10, 50 and 100 at a current density of 37 mA g^{-1} for (a) GO, (b) rGO$_{700Ar/H2}$ and (c) rGO$_{1000Ar/H2}$ (U$_{LTC}$ = lower termination criterion and U$_{UTC}$ = upper termination criterion).

graphite-typical stages can be observed during the (de-) lithiation reaction due to the lack of long-range order (see Fig. 2a). It should be noted that the voltage hysteresis is at a remarkably low level, indicating that the capacity results mainly from intercalation within the graphitic lattice.

The post-mortem XPS measurements prove that the functional groups of the (r)GO material influence the SEI composition. Next to the above mentioned "dead" Li$_x$C also the C=O signal (at ~288 eV[61,62]) of the C 1s spectra (see Fig. S3 in the supplementary information), which is mainly attributed to Li$_2$CO$_3$, gets significantly reduced with increasing reduction degree. Li$_2$CO$_3$ is no product of the initial reduction reaction of carbonate-based electrolytes during SEI formation, but a product of secondary reactions of lithium ethylene decarbonate (LEDC).[71] Hence, our results imply that the stability of LEDC is decreased by the presence of O-functionalizations.

The results shown in Fig. 6 are in good agreement with the findings of Kuo et al.,[21] where similar results are presented for one lithiation-delithiation cycle. However, the behavior during further cycling is of crucial importance for the use as matrix material in high energy anodes. Figure 7 shows the differential capacities for GO, rGO$_{700Ar/H2}$ and rGO$_{1000Ar/H2}$ at cycles 3, 10, 50, and 100 to illustrate the different (de-) lithiation as well as degradation phenomena in more detail.

As shown in Fig. 6, different (de-) lithiation processes of the active material can be observed. For GO, two clearly distinguishable lithiation processes (I$_{lit}$ & II$_{lit}$) can be determined. The intercalation

reaction in the range <0.25 V vs Li/Li$^+$ (II$_{lit}$), which is known for graphitic materials with high long-range order, has only a small contribution to the total capacity during the lithiation process. In contrast, the less reversible lithiation of the functional groups (I$_{lit}$) has a much higher contribution. It has a maximum between 0.25 V and 0.5 V (I$_{lit}$) and also overlaps with the reversible lithiation process of graphite in the range below 0.25 V vs Li/Li$^+$. The described maximum as well as the overlapping range <0.25 V vs Li/Li$^+$ decreases with increasing cycle number, since these processes are known to be semi-reversible.[54,55,72] Furthermore, it is evident that the graphitic (de-) lithiation processes II$_{lit/delith}$ remain stable over 100 cycles at a low peak capacity of 200 mAh gV^{-1}. Consequently, the graphitic portion of the GO structure does not seem to degrade significantly. The delithiation capacity which is related to the functional groups (I$_{delit}$) decreases over 100 cycles. Therefore, a change in the capacity-determining lithiation process can be observed during the cycling of GO. While the semi-reversible (de-) lithiation process (I$_{lit/delit}$) is capacity-determining in the first cycles, this is replaced by the more reversible graphitic lithiation process (II$_{lit/delit}$). Thus, the change in capacity over the cycles shown in Fig. 5a can be attributed to two simultaneous lithiation processes with different degrees of reversibility.

If GO and rGO$_{700Ar/H2}$ are compared in Fig. 5a, the capacity fade is similar, while the achieved specific capacity is higher for rGO$_{700Ar/H2}$. Having a deeper look at the specific differential capacities in contrast to GO no clear maximum at 0.3 V vs Li/Li$^+$ can be detected for rGO$_{700Ar/H2}$ during lithiation as a result of the strong reduction of the functional groups. Similar to GO, an increase in capacity change is observed in the range <0.25 V vs Li/Li$^+$ (II$_{lit}$). Due to the increased number of C=C sp^2 bonds (see Fig. 4a), a reversible graphitic lithiation process can be assumed. As already observed for GO, lithiation of the functional groups occurs over the entire voltage range in addition to the main reaction (I/II$_{lit}$). The delithiation process of the functional groups in rGO$_{700Ar/H2}$ (I$_{delit}$ at 1.2 V vs Li/Li$^+$ in Fig. 7b) is similar to the delithiation of the functional groups in GO (I$_{delit}$ at 1.4 V in Fig. 7a), even though no obvious I$_{lit}$ peak is visible for rGO$_{700Ar/H2}$ (Fig. 7b). This suggests that the lithiation process of the oxygen-containing functional groups is superimposed by the lithiation of the more reversible groups and decreases with increasing number of cycles. Notably, the delithiation potential of I$_{delit}$ is decreased from 1.4 V (for GO) to 1.2 V (for rGO$_{700Ar/H2}$). This may be a result of a decreased electrostatic attraction of lithium ions due to the reduced amount of functional groups.[72] Furthermore, a shift of the graphitic delithiation II$_{delit}$ can be observed during cycling. A possible explanation could be the higher surface-to-volume ratio of rGO$_{700Ar/H2}$ compared to GO and rGO$_{1000Ar/H2}$ (see Fig. 2c). This high surface area combined with the remaining functionalization enables a higher amount of surface reactions with the electrolyte. This may result in an increased formation of the passivation layer, which in turn promotes the voltage shift and the loss of capacity.[72] The higher mass fraction of active material, which can be lithiated reversibly, causes the higher total capacity for rGO$_{700Ar/H2}$ compared to GO (see Fig. 5a), yet fading behavior is similar.

This hypothesis is strengthened by the (de-) lithiation behavior of rGO$_{1000Ar/H2}$. In both the lithiation and delithiation reaction, only the fraction of highly reversible lithiation capacity (II$_{lit/delit}$) is evident. Over the entire number of cycles, the (de-) lithiation profiles do not differ, since no non-reversible side reaction with functional groups (I$_{lit/delit}$) occurs. Nevertheless, some functional groups are still present in rGO$_{1000Ar/H2}$ (see Figs. 1f and 3a), which influence the (de-) lithiation behaviour. However, it can be assumed that these are mainly H-terminated and therefore highly reversible.[56] Furthermore, compared to graphite the amorphous parts in rGO$_{1000Ar/H2}$ (see Fig. 2a) lead to a lower capacity, as known for soft carbon materials.[23] Therefore, the highly reversible capacity on that low level can be explained by a combination of the structural differences and the absence of functional groups, which cannot be lithiated reversibly.

Table II. Summary of electrochemical properties from galvanostatic cycling vs Li/Li$^+$.

Properties	Unit	GO	rGO$_{RSD}$	rGO$_{700Ar}$	rGO$_{700Ar/H2}$	rGO$_{1000Ar/H2}$
Delithiation capacity cycle$_{1-100}$	Ah g^{-1}	24.3	26.9	29.9	30.8	20.7
Irreversible capacity cycle$_1$	mAh g^{-1}	1710	1225	764	444	420
CE cycle$_1$	%	21.6	29.3	40.2	54.4	34.8
Average CE cycle$_{2-50}$		95.1	93.5	97.9	98.5	96.7
Average CE cycle$_{51-100}$		97.6	94.6	99.3	99.5	99.0

Table II summarizes the most important electrochemical properties in terms of galvanostatic cycling versus lithium as counter electrode. Using the coulombic efficiencies shown in Table II, it is possible to quantify the (ir-) reversible capacity changes during cycling. However, to determine the reactions causing an irreversible capacity loss, it is necessary to consider the capacity changes as a function of voltage, as shown in Figs. 5 and 6.

Conclusions

In this study, we investigated the influence of thermal post-reduction of rGO prepared via reactive spray drying technique (rGO$_{RSD}$) on various physico-chemical properties as well as on the electrochemical behavior in terms of (de-) lithiation. For this purpose, rGO$_{RSD}$ was post-treated in argon or argon/hydrogen for 2 h at 700 °C (rGO$_{700Ar}$/rGO$_{700Ar/H2}$) and 1000 °C (rGO$_{1000Ar/H2}$).

By increasing the reduction temperature and with hydrogen-containing atmosphere, the functional groups in GO were successively removed from the carbon lattice. As a result of the restoration of the π-π*-electron system, the electrical conductivity increased with decreasing oxygen content. Temperature treatments at 700 °C led to the formation of a crystalline structure with greater long-range order, independent of hydrogen in the atmosphere. In contrast, this long-range order again decreased at a temperature of 1000 °C. In addition, due to interaction of exfoliation and particle coarsening effects a maximum in BET surface area of 133 m^2 g^{-1} was found for rGO$_{700Ar}$.

As reported in literature, the surface area should have a major impact on SEI formation and thus on the irreversible capacity during the first lithiation. In contrast, we observed a linear increase in irreversible capacity with increasing oxygen content in rGO. This demonstrates that the oxygen content has a significantly higher contribution to the capacity loss compared to the specific surface area due to non-reversible reactions of oxygen containing functional groups with the electrolyte components.

As a result of these reactions, the specific capacities of GO, rGO$_{RSD}$, rGO$_{700Ar}$ and rGO$_{700Ar/H2}$ decrease continuously. We point out that two different (de-) lithiation processes take place in reduced graphene oxide matrices at different potentials.

On the one hand, a highly reversible (de-) intercalation process into the graphitic structures and, on the other hand, faradaic reactions of functional groups, which decrease continuously with the number of cycles.

Due to their higher binding energies, the delithiation of functional groups requires a higher voltage than the deintercalation of lithium from graphite, which explains their strong hysteresis effect. For this reason, we draw attention to the fact that an increase in specific capacity due to the presence of functional groups does not have a direct correlation with an increase in power density in full-cell applications. Contrary to the trend of all other electrochemical results we observe a constant delithiation capacity for rGO$_{1000Ar/H2}$ and the by far lowest lithiation-delithiation potential hysteresis.

At this degree of reduction, the physico- and electrochemical properties of rGO are changed to such an extent that they correspond to those of typical soft carbons. Nevertheless, the specific capacity of rGO$_{1000Ar/H2}$ is the lowest of all materials over the entire 100 cycles. This is due to the interaction of two aspects. Firstly, the further removal of O-containing groups from rGO results in a loss of long-range order within the lattice, while the thermal energy is not yet sufficient to properly anneal the defects of the soft carbon-like structure. Secondly, the faradaic reactions of the functional groups almost no longer contribute to the total capacity.

Based on our results, it becomes evident that rGO in its various stages of reduction towards soft carbon will not outperform the commonly applied commercial anode materials in terms of cycle stability and specific capacity. However, we certainly see potential in applications where the high specific surface area as well as the properties of the functional groups can be advantageous. An example would be the use in lithium-sulfur batteries to suppress the polysulfide shuttle.[73]

Another application could be silicon-carbon composites where only partial lithiation of the silicon particles is desired.[74] Compared to graphite, rGO offers the advantage of a higher surface-to-volume ratio combined with high mechanical flexibility. Therefore, an increase in energy density can be achieved by using rGO.

ORCID

S. Müllner ⓘ https://orcid.org/0000-0001-9696-0011
T. Held ⓘ https://orcid.org/0000-0003-3333-2944
T. Tichter ⓘ https://orcid.org/0000-0001-6773-9617
P. Rank ⓘ https://orcid.org/0009-0008-5334-5578
C. Roth ⓘ https://orcid.org/0000-0003-1159-2956

References

1. M. R. Al Hassan, A. Sen, T. Zaman, and M. S. Mostari, *Materials Today Chemistry*, **11**, 225 (2019).
2. G. Jo, M. Choe, S. Lee, W. Park, Y. H. Kahng, and T. Lee, *Nanotechnology*, **23**, 112001 (2012).

3. E. Yoo, J. Kim, E. Hosono, H. Zhou, T. Kudo, and I. Honma, *Nano Lett.*, **8**, 2277 (2008).
4. P. Guo, H. Song, and X. Chen, *Electrochem. Commun.*, **11**, 1320 (2009).
5. S. Müllner, T. Held, A. Schmidt-Rodenkirchen, T. Gerdes, and C. Roth, *J. Electrochem. Soc.*, **168**, 120545 (2021).
6. X. Zhou, Y.-X. Yin, L.-J. Wan, and Y.-G. Guo, *Chemical communications (Cambridge, England)*, **48**, 2198 (2012).
7. Y. J. Mai, X. L. Wang, J. Y. Xiang, Y. Q. Qiao, D. Zhang, C. D. Gu, and J. P. Tu, *Electrochim. Acta*, **56**, 2306 (2011).
8. X. Zhu, Y. Zhu, S. Murali, M. D. Stoller, and R. S. Ruoff, *ACS Nano*, **5**, 3333 (2011).
9. K. S. Novoselov, A. K. Geim, S. V. Morozov, D. Jiang, Y. Zhang, S. V. Dubonos, I. V. Grigorieva, and A. A. Firsov, *Science (New York, N.Y.)*, **306**, 666 (2004).
10. N. Kumar, R. Salehiyan, V. Chauke, O. Joseph Botlhoko, K. Setshedi, M. Scriba, M. Masukume, and S. Sinha, *Ray, FlatChem*, **27**, 100224 (2021).
11. V. Agarwal and P. B. Zetterlund, *Chem. Eng. J.*, **405**, 127018 (2021).
12. A. M. Dimiev and S. Eigler (ed.), *Graphene oxide: Fundamentals and applications* (West Sussex, Wiley, Incorporated, Chichester) (2017).
13. W. S. Hummers and R. E. Offeman, *J. Am. Chem. Soc.*, **80**, 1339 (1958).
14. W. Cai et al., *Science (New York, N.Y.)*, **321**, 1815 (2008).
15. I. Jung et al., *J. Phys. Chem. C*, **113**, 18480 (2009).
16. E. F. Sheka, I. Natkaniec, V. Mel'Nikov, and K. Druzbicki, *Nanosystems: Physics, Chemistry, Mathematics*, **6**, 378 (2015).
17. V. O. Kotsyubynsky, V. M. Boychuk, I. M. Budzulyak, B. I. Rachiy, M. A. Hodlevska, A. I. Kachmar, and M. A. Hodlevsky, *Adv. Nat. Sci.: Nanosci. Nanotechnol.*, **12**, 35006 (2021).
18. I. Sengupta, S. Chakraborty, M. Talukdar, S. K. Pal, and S. Chakraborty, *J. Mater. Res.*, **33**, 4113 (2018).
19. S. Hun, *Physics and Applications of Graphene - Experiments*, ed. S. Mikhailov (Rijeka, InTech) (2011).
20. A. Ganguly, S. Sharma, P. Papakonstantinou, and J. Hamilton, *J. Phys. Chem. C*, **115**, 17009 (2011).
21. S.-L. Kuo, W.-R. Liu, C.-P. Kuo, N.-L. Wu, and H.-C. Wu, *J. Power Sources*, **244**, 552 (2013).
22. J. M. Tarascon and M. Armand, *Nature*, **414**, 359 (2001).
23. A. Pendashteh, B. Orayech, H. Suhard, M. Jauregui, J. Ajuria, B. Silván, S. Clarke, F. Bonilla, and D. Saurel, *Energy Storage Mater.*, **46**, 417 (2022).
24. D. Xiong, X. Li, H. Shan, Y. Zhao, L. Dong, H. Xu, X. Zhang, D. Li, and X. Sun, *Electrochim. Acta*, **174**, 762 (2015).
25. J. W. Weber, V. E. Calado, and M. C. M. van de Sanden, *Appl. Phys. Lett.*, **97**, 91904 (2010).
26. C. Zöllner and D. Brueggemann, *Optical and Analytical Studies on DPF Soot Properties and Consequences for Regeneration Behavior* (United States, SAE International) (2017).
27. L. Klemeyer, H. Park, and J. Huang, *ACS Materials Lett.*, **3**, 511 (2021).
28. V. O. Kotsyubynsky, V. M. Boychuk, I. M. Budzuliak, B. I. Rachiy, R. I. Zapukhlyak, M. A. Hodlevska, A. I. Kachmar, O. R. Bilogubka, and A. A. Malakhov, *Adv. Nat. Sci: Nanosci. Nanotechnol*, **22**, 31 (2021).
29. X. H. Yau, F. W. Low, C. S. Khe, C. W. Lai, S. K. Tiong, and N. Amin, *PLoS One*, **15**, e0228322 (2020).
30. K. Bu, J.-T. Wang, H. Weng, and C. Chen, *Phys. Rev. B*, **101**, 205104 (2020).
31. O. Elomaa, V. K. Singh, A. Iyer, T. J. Hakala, and J. Koskinen, *Diam. Relat. Mater.*, **52**, 43 (2015).
32. S. N. Alam, N. Sharma, and L. Kumar, *Graphene*, **06**, 1 (2017).
33. L. Stobinski, B. Lesiak, A. Malolepszy, M. Mazurkiewicz, B. Mierzwa, J. Zemek, P. Jiricek, and I. Bieloshapka, *J. Electron. Spectrosc. Relat. Phenom.*, **195**, 145 (2014).
34. G. Çakmak and T. Öztürk, *Diam. Relat. Mater.*, **96**, 134 (2019).
35. Z. Q. Li, C. J. Lu, Z. P. Xia, Y. Zhou, and Z. Luo, *Carbon*, **45**, 1686 (2007).
36. R. Rozada, J. I. Paredes, S. Villar-Rodil, A. Martínez-Alonso, and J. M. D. Tascón, *Nano Res.*, **6**, 216 (2013).
37. R. Rozada, J. I. Paredes, M. J. López, S. Villar-Rodil, I. Cabria, J. A. Alonso, A. Martínez-Alonso, and J. M. D. Tascón, *Nanoscale*, **7**, 2374 (2015).
38. P. Chen, H. Li, S. Song, X. Weng, D. He, and Y. Zhao, *Results in Physics*, **7**, 2281 (2017).
39. X. Jiao, Y. Qiu, L. Zhang, and X. Zhang, *RSC Adv.*, **7**, 52337 (2017).
40. M. Strankowski, D. Włodarczyk, and J. Piszczyk, *Strankowska, Journal of Spectroscopy*, **2016**, 1 (2016).
41. S. Müllner, T. Michlik, M. Reichel, T. Held, R. Moos, and C. Roth, *Batteries*, **9**, 248 (2023).
42. C. Thomsen and S. Reich, *Phys. Rev. Lett.*, **85**, 5214 (2000).
43. F. Tuinstra and J. L. Koenig, *J. Chem. Phys.*, **53**, 1126 (1970).
44. M. Oschatz, P. Pré, S. Dörfler, W. Nickel, P. Beaunier, J.-N. Rouzaud, C. Fischer, E. Brunner, and S. Kaskel, *Carbon*, **105**, 314 (2016).
45. H. Yang et al., *ACS Nano*, **14**, 6249 (2020).
46. T.-F. Yeh, J.-M. Syu, C. Cheng, T.-H. Chang, and H. Teng, *Adv. Funct. Mater.*, **20**, 2255 (2010).
47. K. Gross, J. J. P. Barragán, S. Sangiao, J. M. de Teresa, L. Lajaunie, R. Arenal, H. A. Calderón, and P. Prieto, *Nanotechnology*, **27**, 365708 (2016).
48. G. Eda, C. Mattevi, H. Yamaguchi, H. Kim, and M. Chhowalla, *J. Phys. Chem. C*, **113**, 15768 (2009).
49. X. Huang, F. Liu, P. Jiang, and T. Tanaka, *IEEE International Conference on Solid Dielectrics (ICSD)*, **2013**, 904 (2013).
50. N. V. Kurnosov, A. S. Linnik, and V. A. Karachevtsev, *Low Temp. Phys.*, **46**, 285 (2020).
51. C. Sauter, R. Zahn, and V. Wood, *J. Electrochem. Soc.*, **167**, 100546 (2020).
52. M.-S. Wu, T.-L. Liao, Y.-Y. Wang, and C.-C. Wan, *J. Appl. Electrochem.*, **34**, 797 (2004).
53. M. Kirchhöfer, J. von Zamory, E. Paillard, and S. Passerini, *Int. J. Mol. Sci.*, **15**, 14868 (2014).
54. J. Collins, G. Gourdin, M. Foster, and D. Qu, *Carbon*, **92**, 193 (2015).
55. W. Xing and J. R. Dahn, *J. Electrochem. Soc.*, **144**, 1195 (1997).
56. D. Yoon, K. Y. Chung, W. Chang, S. M. Kim, M. J. Lee, Z. Lee, and J. Kim, *Chem. Mater.*, **27**, 266 (2015).
57. M. Schroeder, M. Winter, S. Passerini, and A. Balducci, *J. Power Sources*, **238**, 388 (2013).
58. B. Babu, P. Simon, and A. Balducci, *Adv. Energy Mater.*, **10**, 2001128 (2020).
59. J. R. Dahn, T. Zheng, Y. Liu, and J. S. Xue, *Science*, **270**, 590 (1995).
60. J. R. Dahn, A. K. Sleigh, H. Shi, J. N. Reimers, Q. Zhong, and B. M. Way, *Electrochim. Acta*, **38**, 1179 (1993).
61. V. Sharova, A. Moretti, T. Diemant, A. Varzi, R. Behm, and S. Passerini, *J. Power Sources*, **375**, 43 (2018).
62. C. Fang et al., *Nature*, **572**, 511 (2019).
63. Y. Cui, S. Liu, B. Liu, D. Wang, Y. Zhong, X. Zhang, X. Wang, X. Xia, C. Gu, and J. Tu, *Front. Chem.*, **7**, 952 (2019).
64. A. Lahiri, N. Borisenko, A. Borodin, M. Olschewski, and F. Endres, *Physical chemistry chemical physics PCCP*, **18**, 5630 (2016).
65. F. La Mantia and P. Novák, *Electrochem. Solid-State Lett.*, **11**, A84 (2008).
66. H. Buqa, A. Würsig, J. Vetter, M. E. Spahr, F. Krumeich, and P. Novák, *J. Power Sources*, **153**, 385 (2006).
67. R. Lundström, N. Gogoi, X. Hou, and E. J. Berg, *J. Electrochem. Soc.*, **170**, 40516 (2023).
68. V. S. Channu, R. Bobba, and R. Holze, *Colloids Surf., A*, **436**, 245 (2013).
69. T. Zheng, J. S. Xue, and J. R. Dahn, *Chem. Mater.*, **8**, 389 (1996).
70. T. Zheng, W. R. McKinnon, and J. R. Dahn, *J. Electrochem. Soc.*, **143**, 2137 (1996).
71. S. K. Heiskanen, J. Kim, and B. L. Lucht, *Joule*, **3**, 2322 (2019).
72. E. Frackowiak, S. Gautier, H. Gaucher, S. Bonnamy, and F. Beguin, *Carbon*, **37**, 61 (1999).
73. Q. Pang, X. Liang, C. Y. Kwok, and L. F. Nazar, *Nat. Energy*, **1**, 1 (2016).
74. M. Graf, C. Berg, R. Bernhard, S. Haufe, J. Pfeiffer, and H. A. Gasteiger, *J. Electrochem. Soc.*, **169**, 20536 (2022).